Synergistic role of *p-d* hybridization and magnetism in enhanced water splitting on ferromagnetic 1*T* transition metal dichalcogenides

Yuyuan Huang,[1] Shunfang Li,[2,*] Zhenyu Zhang,[1,3] and Ping Cui[†]
[1]*International Center for Quantum Design of Functional Materials (ICQD), Hefei National Research Center for Physical Sciences at the Microscale, University of Science and Technology of China, Hefei, Anhui 230026, China*
[2]*Key Laboratory of Material Physics, Ministry of Education, School of Physics and Microelectronics, Zhengzhou University, Zhengzhou 450001, China*
[3]*Hefei National Laboratory, University of Science and Technology of China, Hefei, Anhui 230088, China*

(Received 24 September 2023; revised 24 February 2024; accepted 23 April 2024; published 6 May 2024)

Orbital hybridization within the *d*-band model has been widely recognized as an important factor affecting the catalytic properties of materials. Separately, the spin degrees of freedom have also been gaining increasing attention in catalytic processes on magnetic substrates. Here, using first-principles calculations based on density functional theory, we systematically investigate the catalytic activity of ferromagnetic MX_2 (M = V, Cr, Mn; X = Se, Te) in the 1*T* phase, focusing on water splitting. Our studies show that 1T-VSe_2 and 1T-VTe_2 are excellent catalysts for the crucial constituent steps of hydrogen evolution reaction (HER) and oxygen evolution reaction (OER), respectively. The enhanced reactivities in these two systems over the other four counterparts can be traced to the synergistic effects of magnetism and strong hybridization between the *p* orbitals of X and *d* orbitals of V. We also propose a modified descriptor of $\Delta_{\sigma\sigma^*}$ to characterize the HER activity, defined by the bonding and antibonding energy splitting, and further demonstrate that the magnetic properties of the catalysts should be explicitly accounted for in both reactions. The present findings may shed light on a microscopic understanding of the physical mechanisms of various catalytic reactions on two-dimensional magnets.

DOI: 10.1103/PhysRevB.109.195414

I. INTRODUCTION

Global warming caused by the greenhouse effect has become a widespread concern of the scientific community and society. The development of sustainable energy technologies, including electrochemical water splitting, has become consequently vitally important. The sluggish kinetics of the two key half-reactions of water splitting, hydrogen evolution reaction (HER) and oxygen evolution reaction (OER), can be effectively promoted by introducing efficient catalysts [1–3]. In this field, a descriptor-based approach to predict the catalytic activity of materials has been well developed, upon which a volcanic-type curve of the catalytic performance is usually correlated by the descriptor [4–9]. For example, the free energy of a hydrogen adsorption (denoted as ΔG_{H^*}) is considered to be a good descriptor of the activity of HER catalysts [4], while the free-energy difference between OH^* and O^* adsorptions ($\Delta G_{OH^*} - \Delta G_{O^*}$) [8] and other descriptors such as the e_g-orbital filling [7] can well describe the activity of OER catalysts. The deeper physical foundations of these descriptors mainly lie in the intrinsic properties of the materials that can lead to differences in adsorption energy. For a single adsorption process on a transition metal (TM) surface, the *d*-band model has been well recognized to be instructive and powerful in describing the differences in adsorption energy, due to the fact that a highly localized *d* orbital influences the most on the bond hybridization, charge transfer, and adsorption [10–15]. In general, since complex catalytic processes may consist of multiple adsorption steps, the *d*-band model and Sabatier principle jointly determine the catalytic performance of TM-based materials [9]. Under such a physical framework, the catalytic efficiency of precious metal catalysts was usually found to stand on the peak of the catalytic volcanic curve, such as Pt being one of the best catalysts for HER and IrO_2 being an excellent catalyst for OER under acidic conditions [3,16].

Besides TM catalysts, some surfaces terminated with atoms whose valence electrons occupy *p* orbitals have also been reported to be catalytically reactive. Here, in analogy to the *d*-band model, a *p*-band center has been proposed as an effective catalytic descriptor, such as in double perovskites [17–19]. In addition, attentions have been paid to the effects of hybridization of *d* and *p* orbitals on the catalytic processes [20–23]. For example, in perovskite systems, regulating the number of oxygen vacancies can change the degree of hybridization between the *d* and *p* orbitals, thereby improving the catalytic activities in HER and OER [20,21]. A physical picture that emphasizes electron exchange between the *d* and *p* orbitals has also been proposed in describing HER processes of defective MoS_2 [22]. Compared to the localized *d* orbitals, the relatively delocalized *p* orbitals are accompanied by weakened adsorption. Thus, the effective *p-d* hybridization between the *p*-block elements and the *d*-block TM elements with relatively high *d*-band center is expected to

*Corresponding author: sflizzu@zzu.edu.cn
†Corresponding author: cuipg@ustc.edu.cn

result in superior catalysts that can compete with noble metals such as Pt and Pd [23]. However, to the best of our knowledge, such a conceptual proposal has not been fully exploited, which nevertheless is potentially instructive in high-efficiency and low-cost catalyst design and fabrication.

So far, our discussions of the catalytic processes have been solely focused on the electron degrees of freedom. Separately, the spin degrees of freedom have also been gaining increasing attention in catalytic processes on magnetic substrates. For example, the initial sticking coefficient of a dissociative O_2 molecule on the Al(111) surface is better interpreted by invoking Wigners spin selection rule [24], but applied in chemical reaction [25–27]. Although the validity of such a physical picture emphasizing spin selection is still debatable [28], more efforts have been focused on the spin degrees of freedom or magnetism in specific catalytic processes [29–39]. For instance, the spin selection rule has been shown to be operative in single atom catalysis (SAC), revealing various novel effects in CO oxidation reaction or other catalytic processes [30,32,39]. More importantly, in the processes of HER and OER, it has been established experimentally that the catalytic effects can be enhanced by applying a magnetic field or tuning the spin states of the catalysts, convincingly demonstrating that consideration of the electronic degrees of freedom of the catalysts alone is insufficient to completely characterize the catalytic processes involved [29,31,33–38].

In this paper, we present a systematical investigation of the catalytic efficiency and mechanism of ferromagnetic 1T-MX_2 (M = V, Cr, Mn; X = Se, Te) for water splitting reactions using first-principles calculations. Such two-dimensional (2D) magnetic metals discovered experimentally may serve as platforms for exploration of catalytic processes [40–43], not only because of their exceptionally high surface-reactive areas, but also for the possibility to integrate the merits of p-electron dominance and magnetism. We predict that 1T-VSe_2 and 1T-VTe_2 are excellent catalysts for the crucial constituent steps of HER and OER, respectively. The enhanced catalytic performance in these two systems over the other four counterparts can be traced to the synergistic effects of magnetism and strong hybridization between the p orbitals of X and d orbitals of V. For HER, we demonstrate that the catalytic activities of these 1T-MD systems are dominated by the p_z orbitals of anions with p-d hybridization, and further propose a modified descriptor of $\Delta_{\sigma\sigma^*}$ defined by the bonding and antibonding energy splitting to characterize the catalytic activity. Thus, 1T-VSe_2 exhibits superior HER catalytic performance due to the appropriate position of its p_z orbital center and strong p-d hybridization around the Fermi level. We further reveal that the magnetic properties of the catalysts should be explicitly accounted for, indicating the joint effects of orbital hybridization and spin degrees of freedom. Moreover, unlike the HER, the strong p-d hybridization near the Fermi level leads to strong binding with the highly electronegative O atoms. But analogous to HER, the magnetic degrees of freedom in the OER are again cooperatively involved, specifically, in the reaction process of O^* adsorption on 1T-VTe_2. The present findings on p-d-hybridization-dominated and magnetism-enhanced catalytic activities are expected to provide perspectives for developing high-performance catalysts based on 2D magnets.

This paper is organized as follows. The methods and details of first-principles calculations are introduced in Sec. II. The results and discussion of the electronic and catalytic properties are presented in Sec. III. Finally, we present a brief summary in Sec. IV.

II. COMPUTATIONAL DETAILS

We performed first-principles calculations based on density functional theory (DFT) implemented in the Vienna *Ab initio* Simulation Package (VASP) [44–46]. Projector augmented wave (PAW) was employed with an energy cutoff set to be 600 eV [47,48]. Generalized gradient approximation in the Perdew-Burke-Ernzerhof formalism was used to describe the electron exchange and correlation energy [49]. To describe the 2D magnetic system, spin-polarized calculations with van der Waals interactions corrected by the DFT-D3 method were employed [50]. A $4 \times 4 \times 1$ supercell with more than 15 thick vacuum space were used to avoid coupling between periodic structures. The total energy convergence criterion was set to $10^{-}5$ eV and the force convergence criteria for structure optimization was set to be 0.01 eV/Å. To simulate more realistic magnetic correlation systems, different effective on-site Coulomb interaction parameters (U_{eff} = 2, 3, 4 for V, Cr, Mn, respectively) were adopted according to the previous studies [51–53]. For a deeper understanding of the bonding and antibonding between the catalyst and the intermediate in these two chemical reactions, we used Lobster software for the spin resolved crystal orbital Hamilton population (COHP) analysis [54].

The computational hydrogen electrode (CHE) model was employed to calculate the free energies for both the HER and OER [4]. For the HER in an acid environment, two steps are involved: hydrogen adsorption (Volmer reaction step) and formation of H_2 molecule (Heyrovsky reaction step and Tafel reaction step) [9]. The Gibbs free energy of hydrogen adsorption (ΔG_{H^*}) is usually used to characterize the catalytic activity of a catalyst, which can be expressed by

$$\Delta G_{H^*} = \Delta E_{H^*} + \Delta E_{\mathrm{ZPE}} - T\Delta S, \tag{1}$$

with the binding energy of hydrogen (ΔE_{H^*}) defined by

$$\Delta E_{H^*} = E_{H^*} - \tfrac{1}{2}E_{H_2} - E_{\mathrm{sub}}. \tag{2}$$

vskip-3ptHere, ΔE_{ZPE} and ΔS represent the zero-point energy difference and the entropy difference before and after hydrogen adsorption, respectively; E_{H^*}, E_{H_2}, and E_{sub} are the energies of the combined system of a H atom adsorbed on a substrate, H_2 molecule in gas phase, and the substrate, respectively; T is the temperature, which was set to 298.15 K to simulate the reaction in room temperature. According to the famous volcano curve with ΔG_{H^*} as the horizontal axis, materials with ΔG_{H^*} approaching 0 eV are considered to possess the best HER catalytic activity, while the $\Delta G_{H^*} < 0$ eV and $\Delta G_{H^*} > 0$ eV regions represent stronger and weaker binding of H*, respectively. And the overpotential of HER (η_{HER}) is represented by ΔG_{H^*}/e.

For the OER in alkaline conditions, a four-step process is given as

$$OH^- + * \rightarrow OH^* + e^- \tag{3}$$

$$OH^- + OH^* \rightarrow O^* + e^- + H_2O \tag{4}$$

TABLE I. Lattice constants and magnetic moments of the metal atoms of monolayered 1T-MX_2 with the DFT-D3 method. The lattice constants in previous studies are also shown for comparison.

1T-MX_2	Lattice constant calculated with DFT-D3 (Å)	Lattice constant in previous studies (Å)	Magnetic moments of TMs (μB)
1T−VSe_2	3.42	3.35 (experiment) [55]	1.46
1T−VTe_2	3.64	3.6 (experiment) [56]	1.76
1T−$CrSe_2$	3.44	3.6 (experiment) [43]	3.14
1T−$CrTe_2$	3.68	3.79 (experiment) [42]	3.33
1T−$MnSe_2$	3.63	3.62 (calculation) [57]	3.96
1T−$MnTe_2$	3.82	3.87 (calculation) [58]	4.12

$$OH^- + O^* \rightarrow OOH^* + e^- \quad (5)$$

$$OH^- + OOH^* \rightarrow O_2 + e^- + H_2O \quad (6)$$

Similarly, the Gibbs free energy for each step can be expressed by $\Delta G = \Delta E + \Delta E_{ZPE} - T\Delta S - eU$. Here, e represents the number of electrons participating in the reaction, and U stands for the electrode potential with respect to the standard hydrogen electrode (SHE), which was set to 1.23 V in our calculations. To characterize the possibility of evolution from the previous adsorbate to the next adsorbate, four free energies are defined as $\Delta G_1 = \Delta G_{OH^*}$, $\Delta G_2 = \Delta G_{O^*} - \Delta G_{OH^*}$, $\Delta G_3 = \Delta G_{OOH^*} - \Delta G_{O^*}$,and $\Delta G_4 = \Delta G_{OO^*} - \Delta G_{OOH^*}$. The OER activity can be evaluated by the overpotential η_{OER}, which is defined as

$$\eta_{OER} = \max[\Delta G_1, \Delta G_2, \Delta G_3, \Delta G_4]/e - 1.23V. \quad (7)$$

The most widely used OER volcano curve proposed by Nørskov takes $\Delta G_{OH^*} - \Delta G_{O^*}$ as the horizontal axis, due to the linear relationship between the OER adsorbates [8]. Materials located around the curve peak possess the best catalytic activity. On the left-hand side of the volcano curve, the binding of oxygen is too strong, while on the right-hand side, the binding of oxygen is too weak.

III. RESULTS AND DISCUSSION

A. Electronic properties of 1T-MX_2

1T-MX_2 (M = V, Cr, Mn; X = Se, Te) have sandwich structures with a space group of $P\bar{3}m1$, wherein the d-block M atoms are located in the sandwich home surrounded by the p-block X atoms, forming an octahedral crystal field. The calculated lattice constants of monolayered 1T-MX_2 with the DFT-D3 method are given in Table I, consistent with the experimental and previous theoretical studies [42,43,55–58].

To analyze the electronic properties of monolayered 1T-MX_2, we calculate the band structures and the density of states (DOS). As shown in Fig. 1, all the six systems are of obvious metallicity. Specifically, for 1T-VSe_2 and 1T-VTe_2, the d-electrons of the M atoms dominate the states near the Fermi surface [see Figs. 1(g) and 1(h)]. For 1T-$CrSe_2$ and 1T-$CrTe_2$, the contributions of the d orbitals move downward and are located in the energy range [–2, 0 eV], while for 1T-$MnSe_2$ and 1T-$MnTe_2$, the main peaks of the d-orbital-dominated DOS (d-DOS) sink to a deeper energy window far below the Fermi level [see Figs. 1(i)-1(l)]. Moreover, we also compare the p-orbital-dominated DOS (p-DOS) of these systems. As compared to the d-DOS, the p-DOS are more extended within the range of [–5, 5 eV]. Among them, for the case of 1T-VX_2, the p orbitals of the X atoms hybridize significantly with the d orbitals of the V atoms near the Fermi level. For 1T-CrX_2, the p-d hybridization still exists, which, however, is only observed in a relatively low-energy range as compared to 1T-VX_2, mainly due to the lower-energy range of the d orbitals for the former. In contrast, for 1T-MnX_2, the p orbitals of the X atoms absolutely dominate the DOS near the Fermi level, with merely minor contributions of the d orbitals of the Mn atoms.

The calculated magnetic moments of the M atoms of monolayered 1T-MX_2 are also summarized in Table I. By combining the DOS and magnetic moments, we can estimate the valence states of the M elements using the Hund's rules. Cr and Mn exhibit valence states of +3, while the V atoms show a valence state between +1 and +2, as also manifested by the significant contribution of V to the DOS near the Fermi level. Note that, these 1T-MX_2 systems have been experimentally and theoretically reported to have the long-range ferromagnetic ordering in or near to the monolayer limit with Curie temperatures close to room temperature [40–43,59]. It is worth pointing out that even though a material may not be able to perfectly maintain long-range ferromagnetic ordering at room temperature, it still maintains ferromagnetic properties within a local range due to the higher Curie temperature. For possible AFM states, we also incorporate self-consistent results in Sec. S10 of the Supplemental Material (SM) [62]. Therefore, the relevant properties of these systems in ferromagnetic states can be investigated in this study.

B. HER performance of 1T-MX_2

Now, we investigate the HER catalytic activity of magnetic 1T-MX_2 with the CHE model as introduced in Sec. II. As a starting point, we identify the preferred adsorption site of a H atom on the surface of each 1T-MX_2 to be on top of the X atom by comparing the adsorption energies on different adsorption sites, as detailed in Sec. S1 of the SM [62]. The HER reaction step diagram (Fig. 2) shows that 1T-VSe_2 possesses the lowest ΔG_{H^*} =0.07 eV and is the best catalytic candidate for the HER. Moreover, it is found that for a specific X anion, the adsorption free energy increases with the increase of the atomic number of the M atoms in the periodic table. Alternatively, for a given M element, the 1T-MX_2 consist of the Se anions have a superior HER activity to that with the Te anions. To address the underlying mechanism of the differences in the HER catalytic activity, we analyze charge transfer processes

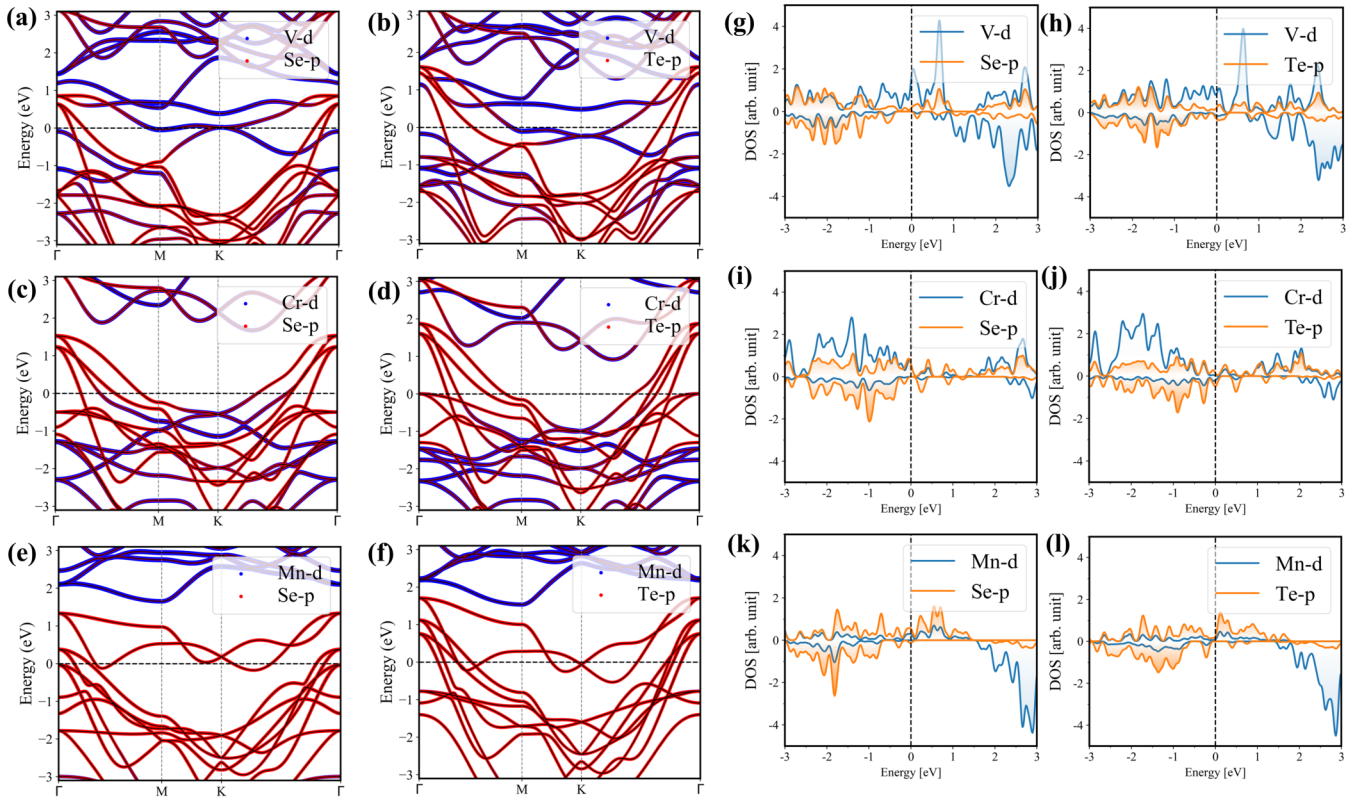

FIG. 1. Projected band structures of (a) 1T-VSe_2, (b) 1T-VTe_2, (c) 1T-$CrSe_2$, (d) 1T-$CrTe_2$, (e) 1T-$MnSe_2$, and (f) 1T-$MnTe_2$. The red and blue data points represent the spectral weights contributed by the metal and chalcogen atoms, respectively. (g)–(l) The corresponding density of states (DOS). The blue and yellow areas represent the contributions from the *d* orbitals of the metal atoms and the *p* orbitals of the chalcogen atoms, respectively.

and changes in the projected DOS (PDOS) after H* adsorption on 1T-MX_2. The charge density differences for all the 1T-MX_2 are shown in Fig. 3, which is defined by

$$\Delta\rho = \rho_{TMX_2+\text{adsorbates}} - \rho_{TMX_2} - \rho_{\text{adsorbates}}, \tag{8}$$

where $\rho_{TMX_2+\text{adsorbates}}$, ρ_{TMX_2} and $\rho_{\text{adsorbates}}$ represent the charge density of the adsorption system, an isolated 1T-MX_2 monolayer and an incoming adsorbate, respectively. Here we differentiate the nearest-neighboring (NN) and distant *M* atoms of the adsorption sites as shown in Fig. S2 within the SM [62]. From Fig. 3, we see that there is an obvious charge density change between the *X* and H atom as well as in the *M*-*X* hybrid regime in each system, due to the hybridization

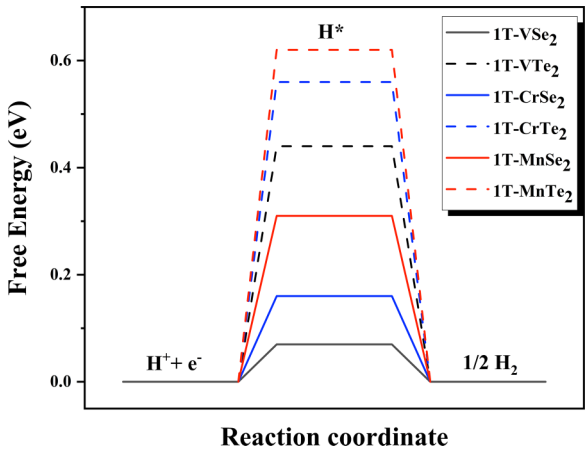

FIG. 2. Calculated free-energy diagram of the HER over 1T-MX_2 in acid media. 1T-VSe_2 exhibits superior HER activity with $\Delta G_{H^*} = 0.07$ eV.

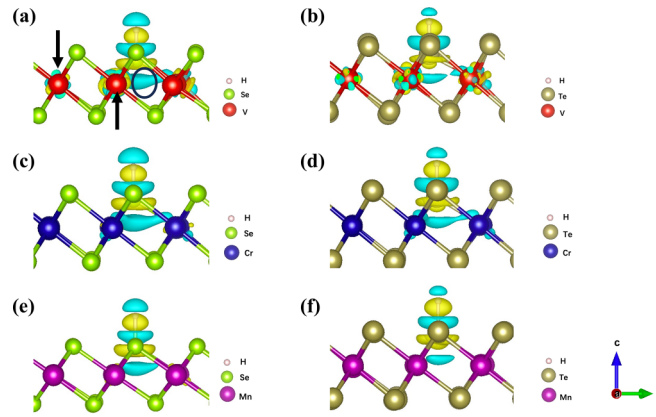

FIG. 3. Charge density differences for H* adsorption on (a) 1T-VSe_2, (b) 1T-VTe_2, (c) 1T-$CrSe_2$, (d) 1T-$CrTe_2$, (e) 1T-$MnSe_2$, and (f) 1T-$MnTe_2$. Blue and yellow areas represent electron depletion and electron and accumulation, respectively. The position marked by the down arrow corresponds to the distant *M* site, while the up arrow highlights the NN *M* atom of the adsorption site, which can refer to Fig. S2 within the SM [62]. The circle highlights significant charge redistribution of the *p*-*d* hybridization region.

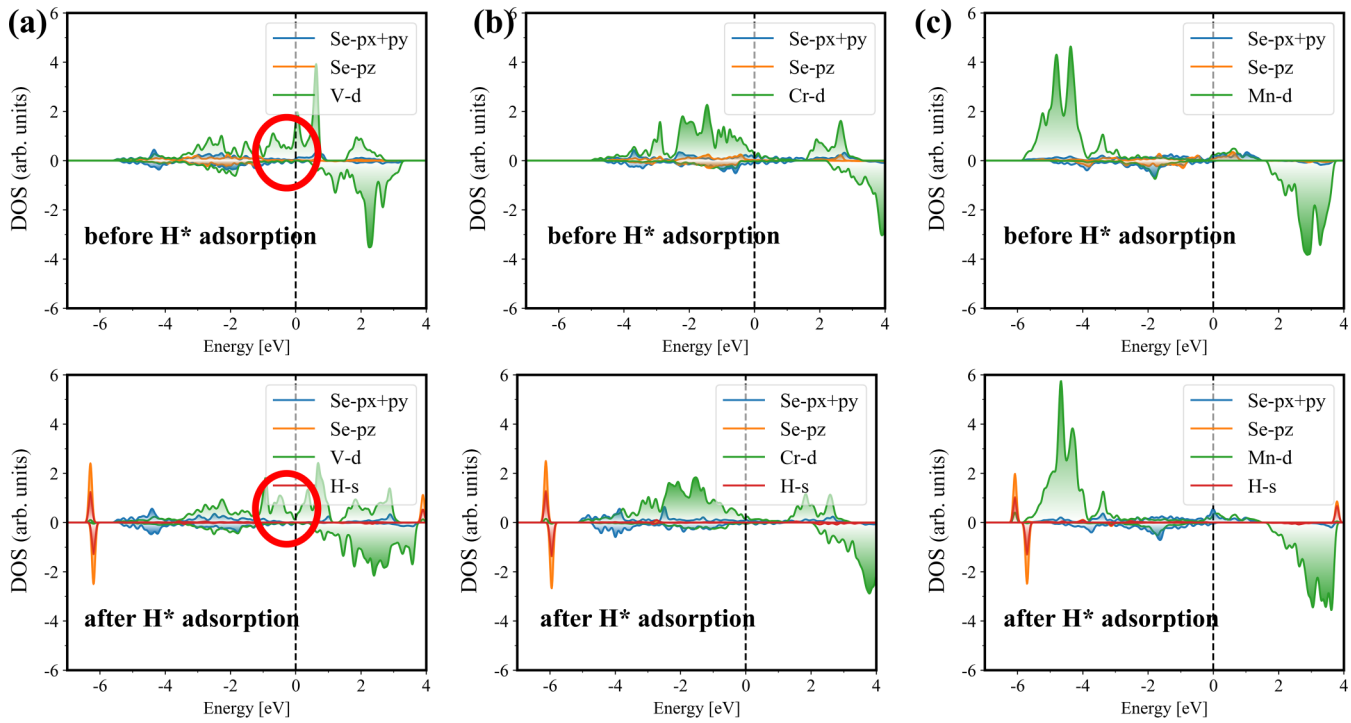

FIG. 4. Projected density of states (PDOS) of the NN M atoms of adsorption sites and the H* adsorbed Se atom before (upper panels) and after (lower panels) H* adsorption on (a) 1T-VSe_2, (b) 1T-$CrSe_2$, and (c) 1T-$MnSe_2$. The red circles highlight significant changes in PDOS of VSe_2 around the Fermi level.

of the p_z orbital of X and the s orbital of H in the formation of the covalent bond and consequently weakening of the NN M-X bonds. In particular, for VX_2, there are also significant charge redistributions on the distant metal atoms, while for the other systems, minimal charge redistribution is observed.

We also present the PDOS of the NN M atoms of the adsorption sites and the H* adsorbed X atoms of 1T-MSe_2 (1T-MTe_2) before and after the H* adsorption in Fig. 4 (Fig. S3 within the SM [62]), which clearly show that in 1T-VX_2, there are significant changes in the d orbitals. Such a feature indicates that although the s orbitals of H hybridizes with the p_z orbitals of X, the d orbitals of V are also highly involved in this process. In contrast, for the cases of 1T-CrX_2 and 1T-MnX_2, the PDOS changes of the d orbitals are not significant, which can be rationalized by the weaker p-d hybridizations compared to the 1T-VX_2 case. As a consequence, upon H* adsorption, the $s-p_z$ hybridization simultaneously results in a rearrangement of the d states. In addition, according to the reconstruction of the distant M atoms charge distribution shown in Fig. 3, we also observe significant PDOS changes of the distant M atoms in 1T-VX_2 and minimal PDOS changes in the other four systems, as shown in Fig. S4 in Sec. S2 of the SM [62]. Collectively, we can draw a self-consistent conclusion that there are significant PDOS changes in both the NN and distant V atoms of the adsorption sites before and after adsorption of H*, and minimal PDOS changes in both the NN and distant Cr/Mn atoms in their respective systems.

Moreover, one can find that, for a given d-block M or p-block X element, the change of ΔG_{H^*} caused by changing the p-block anions is more significant than that for changing the d-block metal atoms. For instance, the HER activity difference between 1T-VSe_2 (0.07 eV) and 1T-VTe_2 (0.44 eV) is much more remarkable compared to that between 1T-VSe_2 and 1T-$CrSe_2$ (0.16 eV) or 1T-$MnSe_2$ (0.31 eV). These findings indicate that the direct s-p interaction between the s orbital of H and the p orbitals of the surface reactive X atoms dominates the H* adsorption, nevertheless the p-d hybridization between the surface p-block X atoms and the sandwiched d-block M atoms also plays a crucial role in H* adsorption and corresponding HER processes.

To provide a more quantitative analysis of the adsorption process of H* on 1T-MX_2, we further calculate the crystal orbital Hamilton population (COHP) between the X and H atoms. The COHP is the overlapping integral of a Hamiltonian matrix of two atoms in a system, with negative and positive values reflecting the bonding and antibonding between the atoms, respectively, and the magnitude of its absolute value reflects the strength of the interaction. As depicted schematically in Fig. 5(a), the interaction between the X and H atoms is similar to the H-H bonding in the formation of H_2, with a significant energy gap between the bonding and antibonding peaks. Since the same bonding law exists in all the six systems, it is possible to analyze the differences between the systems in a unified manner based on this bonding situation. We observe that the energy gaps between the bonding and antibonding energy levels in the six systems exhibit a significant correlation with their catalytic activities. For this reason, we calculate the bonding energy level center E_σ and antibonding energy level center E_{σ^*}, as well as their spacing $\Delta_{\sigma\sigma^*}$,

$$\Delta_{\sigma\sigma^*} = E_{\sigma^*} - E_\sigma = \frac{\int_0^\infty V_{\mathrm{COHP}}(E)EdE}{\int_0^\infty V_{\mathrm{COHP}}(E)dE} - \frac{\int_{-\infty}^0 V_{\mathrm{COHP}}(E)EdE}{\int_{-\infty}^0 V_{\mathrm{COHP}}(E)dE}, \quad (9)$$

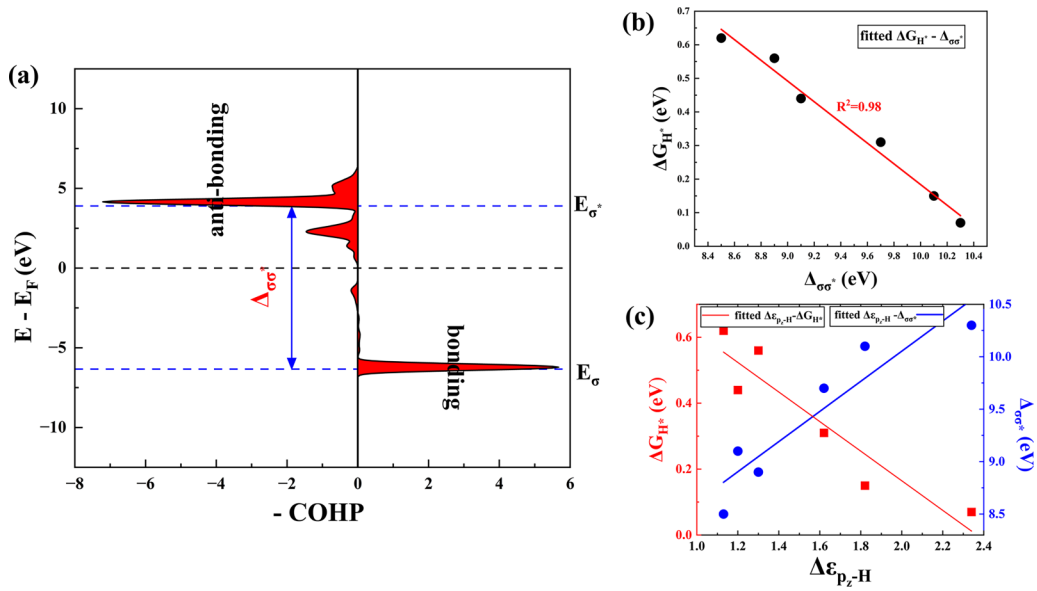

FIG. 5. (a) Schematic diagram of an X-H interaction. The right and left areas with respect to the zero value represent the bonding and antibonding, respectively. The E_σ and E_{σ^*} are the centers of bonding and antibonding states, respectively. $\Delta_{\sigma\sigma^*}$ is the distance between E_σ and E_{σ^*}. (b) ΔG_{H^*} as a function of $\Delta_{\sigma\sigma^*}$. The R-square of the linearly fitted line is 0.98, indicating a significant correlation between the variables. (c) Fitted linear relationships of ΔG_{H^*} and $\Delta\varepsilon_{p_z-H}$ (in red) and $\Delta_{\sigma\sigma^*}$ and $\Delta\varepsilon_{p_z-H}$ (in blue).

where V_{COHP} is the value of COHP and the Fermi level is set to 0 eV. As shown in Fig. 5(b), a nearly linear trend is established between the calculated $\Delta_{\sigma\sigma^*}$ and ΔG_{H^*}, i.e., the larger $\Delta_{\sigma\sigma^*}$ is, the better the HER catalytic activity becomes.

To figure out the physical reason for the direct relationship between $\Delta_{\sigma\sigma^*}$ and ΔG_{H^*}, a simplest molecular orbital theory (MOT) can be invoked. As discussed surrounding Fig. S10 and Sec. S7 within the SM [62], when two isolated equivalent energy levels form a covalent bond, the new antibonding and bonding energy levels move symmetrically up and down in energy, and half of the difference between these two energy levels corresponds to the energy decrease caused by the bond formation. When the two energy levels are not equivalent, the larger their difference, the larger the energy gap between the bonding and antibonding states, resulting in more energy gain upon bonding. Similar to this picture, $\Delta_{\sigma\sigma^*}$ is directly related to ΔG_{H^*}. In analogy to the concept of d-band center model, here we define the center of the p_z-orbital states of each system before H* adsorption ($\varepsilon_{p_z\mathrm{center}}$) as

$$\varepsilon_{p_z\mathrm{center}} = \frac{\int_{-\infty}^{+\infty} \mathrm{PDOS}_{p_z}(E)EdE}{\int_{-\infty}^{+\infty} \mathrm{PDOS}_{p_z}(E)dE}, \tag{10}$$

where $\mathrm{PDOS}_{p_z}(E)$ is the DOS projected onto the p_z orbital of X, characterizing the position of the p_z energy level. The estimation of the initial energy level of the H atom (ε_H) is discussed in Sec. S7 of the SM [62]. As expected, the energy difference $\Delta\varepsilon_{p_z-H} = \varepsilon_H - \varepsilon_{p_z\mathrm{center}}$ exhibits approximately linear relationships with both $\Delta_{\sigma\sigma^*}$ and ΔG_{H^*}, as shown in Fig. 5(c). This means that when the $s-p$ bonding dominates the H* adsorption, the different positions of the p_z center with respect to the H energy level can lead to different intervals between the bonding and antibonding energy levels after adsorption, which ultimately determines the HER catalytic activity (see details in Sec. S7 of the SM [62]). It is noted that, due to the lack of considering the p-d hybridization intensity, only overall approximately linear relationships are obtained.

To demonstrate the importance of ferromagnetism of 1T-VSe_2 in HER, we further investigate the HER activity of both the nonmagnetic (NM) 1T-VSe_2 and the optimized ferromagnetic 1T-VSe_2 structure but with spin polarization off (FM-off). The corresponding calculated Gibbs free energies of hydrogen adsorption are $\Delta G_{H^*-\mathrm{NM}} = 0.23$ eV and $\Delta G_{H^*-\mathrm{FM-off}} = 0.54$ eV, both much larger than that of the ferromagnetic state ($\Delta G_{H^*-\mathrm{FM}} = 0.07$ eV), indicating that the emergence of magnetism significantly enhances the HER activity of the system. Note that magnetization cannot always guarantee benefits for catalysis in different systems, but it can synergistically decrease the H* adsorption energy in the HER catalytic process of 1T-VSe_2. Applying an appropriate external magnetic field can be an alternative way to enhance the HER activity of 1T-VSe_2 even if the magnetism of the system is reduced under some conditions.

C. OER performance of 1T-MX_2

Similar to the H* adsorption, the adsorbates in the OER also prefer to stay on the on-top sites of the X atoms for all the 1T-MX_2. The OER reaction step diagram of each system is shown in Fig. 6, and the corresponding adsorption free energies are presented in Table S2 within the SM [62]. We find a perfect linear relationship between $\Delta G_{\mathrm{OOH}^*}$ and ΔG_{OH^*} for 1T-MX_2 with R-square = 0.998, indicating that the adsorption behavior of the adsorbates on 1T-MX_2 systems is consistent with the framework described by Nørskov [8]. Based on the famous volcano curve with $\Delta G_{\mathrm{OH}^*} - \Delta G_{\mathrm{O}^*}$ as a descriptor [8], 1T-VTe_2 has the catalytic efficiency closest to the top of the volcanic curve and is an efficient catalyst candidate for the OER. The calculated overpotential η_{OER} is

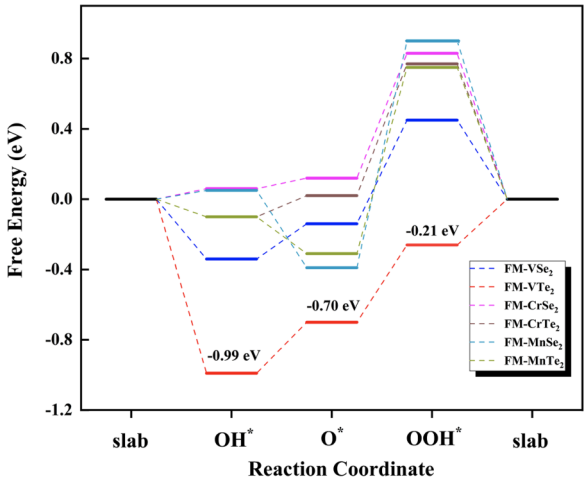

FIG. 6. Calculated free-energy diagram of the OER over 1T-MX_2 under alkaline condition. 1T-VTe_2 exhibits superior OER activity with the overpotential $\eta_{OER} = 0.49$ V.

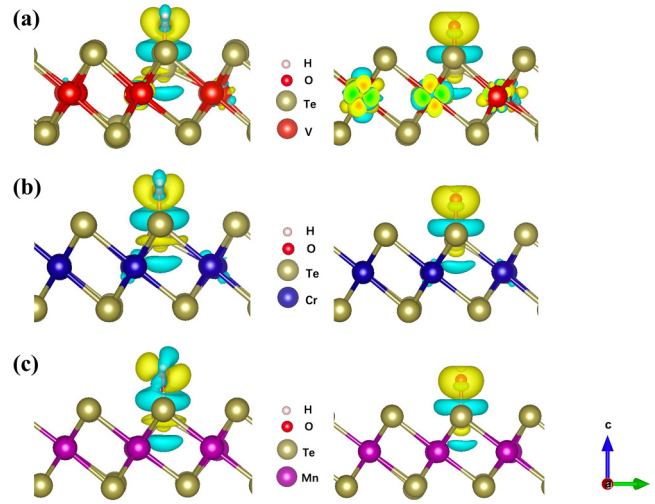

FIG. 7. Charge-density differences diagram for adsorption of OH* (left panels) and O* (right panels) on (a) 1T-VTe_2, (b) 1T-$CrTe_2$ and (c) 1T-$MnTe_2$. Blue and yellow areas represent electron depletion and electron and accumulation, respectively. The positions of the distant M atoms and the NN M atoms of the adsorption site are corresponding to Fig. S2 within the SM [62].

0.49 V, comparable to IrO_2 (about 0.5 V), which is one of the best OER catalyst under acidic conditions and commercially applied [16].

Before further exploring the differences in the OER activity among various systems, we would like to point out that since the OER consists of four steps, the overall catalytic activity is related to these four reactions. Due to the linear relationship between the adsorption of OOH* and OH*, we only consider the adsorption of OH* and O* in the following discussion. From Table S2 within the SM [62], we find that, for the same cation, 1T-MX_2 containing Te atoms have better OER performance than that containing Se atoms. For the same X atom, these systems exhibit catalytic efficiency characteristics of 1T-VX_2 > 1T-CrX_2 > 1T-MnX_2. Specifically, the adsorption free energies of OH* and O* on 1T-VX_2 are significantly lower than that for the other four systems. 1T-CrX_2 and 1T-MnX_2 exhibit a similar behavior when adsorbing OH*, but the adsorption of O* on 1T-MnX_2 is clearly stronger.

Figure 7 shows the charge density differences of 1T-MTe_2 in the OH* and O* adsorption processes, and that for the 1T-MSe_2 systems are displayed in Fig. S6 within the SM [62]. In contrast to the H* adsorption, the adsorption of OH* and O* induces the significant charge transfer from the catalytic 1T-MX_2 substrate to the adsorbates, due to the relatively large electronegativity of O. However, similar to the H* adsorption on 1T-VX_2, upon OH* or O* adsorption, the charge density of the X atom in 1T-VX_2 decreases, with a rearrangement of the charge density around both the distal and NN V atoms of the adsorption sites.

We also calculate the PDOS of the d orbitals and p orbitals of 1T-MTe_2 (1T-MSe_2) systems before and after the OH* or O* adsorption, as shown in Fig. 8 (Fig. S7 within the SM [62]). As expected, significant hybridization between the p orbitals of the X and O atoms are observed. Similar to the HER, the d-DOS of the NN V atoms in 1T-VX_2 changes significantly upon adsorption, while the d-DOS of the NN metal atoms in 1T-CrX_2 and 1T-MnX_2 changes slightly, due to their relatively deeper d-orbital levels. Moreover, similar to the HER process, due to the strong p-d hybridization near the Fermi level, not only the reactive X atom but also all the metal atoms in the entire layer synergistically participate in the catalytic reactions for 1T-VX_2, as manifested by the considerable changes of the d-DOS of the distant V atoms shown in Fig. S8 within the SM [62].

To provide more insights on the charge density variations in the p-d hybridization regime, we calculate ICOHP (integral of the COHP) of the M-X bond before and after a specific reaction. Here, X is the adsorbed surface X atom and M denotes the metal atoms closest to the adsorption site. Such calculations can, to some extent, reflect the M-X bond strength and further characterize the strength of the p-d hybridization. The results are shown in Table S3 within the SM [62], containing the detailed ICOHP changes of M-X during the OER processes. From the table, we see that the ICOHP values for OH* and OOH* are identical, while the ICOHP values for O* are lower than that of OH* and OOH*. These observations are in line with our generic understanding that different strengths of p-d hybridization are involved in the O* or OH*/OOH* adsorption processes, with respectively the number of electrons given by two or one.

Furthermore, to partially reflect the importance of magnetism in determining the catalysis of the present 1T-MX_2 for the OER, here we explore the effects of the adsorption on the magnetic properties of the substrates by comparing their spin-density differences and magnetic moment changes on the magnetic atoms upon OH* and O* adsorptions, as shown in Figs. 9 and 10, respectively. It can be distinctly found that the spin change of each V atom in 1T-VTe_2 is more pronounced than that in the other systems. Usually, the metal atoms closest to the adsorption site (TM7, TM11, and TM12 in Figs. 10 and shown in Fig. S9 and Sec. S6 of the SM [62]) exhibit the most significant spin changes, but in the adsorption on VTe_2, the V atoms relatively far away from the reactive site also exhibit the most significant spin changes (see Figs. 9 and 10, and Tables

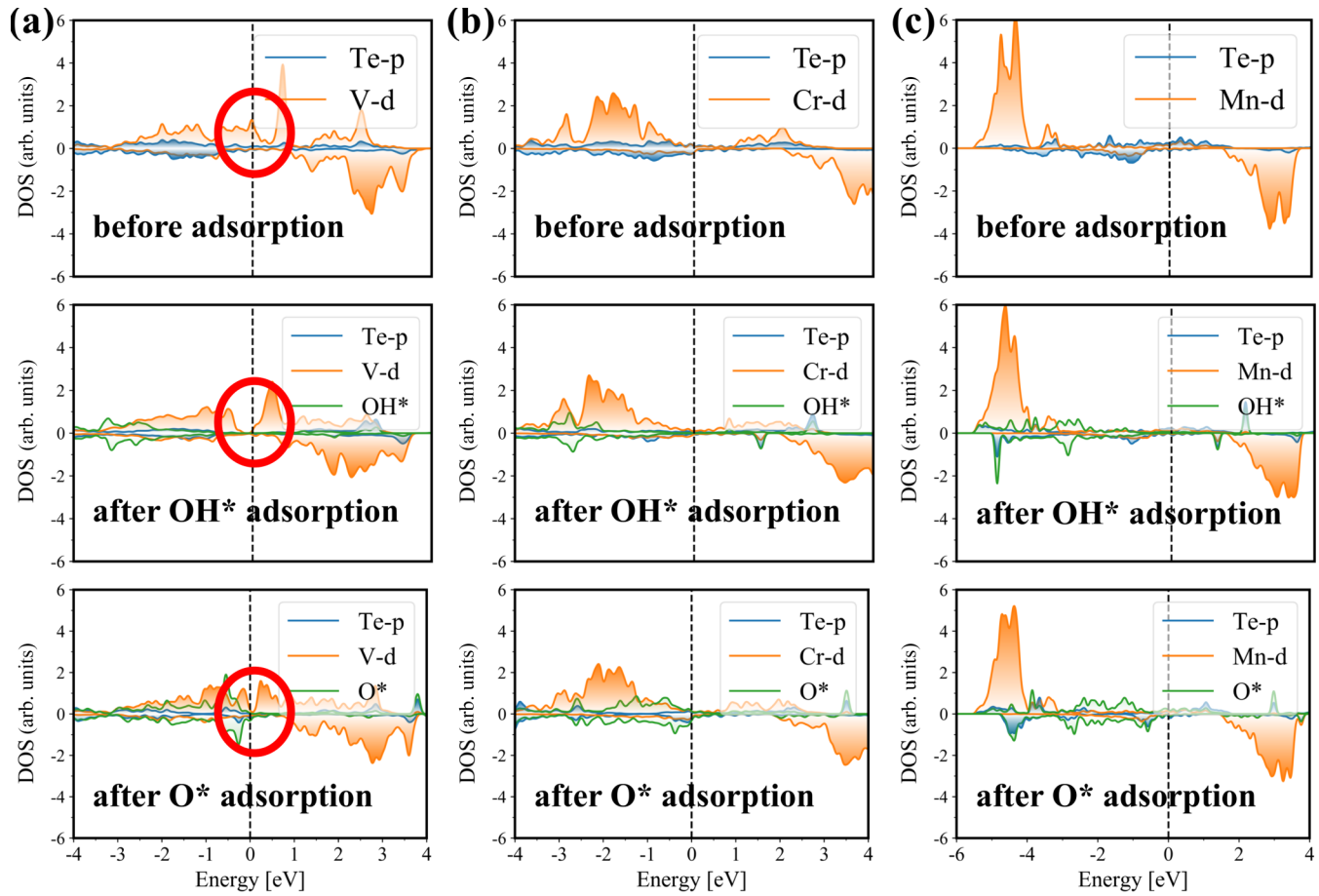

FIG. 8. Projected density of states (PDOS) of the NN TM atoms of the adsorption site and the radical adsorbed Te atom before (upper panels) and after adsorption of OH* (middle panels) and O* (lower panels) on (a) 1T-VTe_2, (b) 1T-$CrTe_2$ and (c) 1T-$MnTe_2$. the red circles highlight significant changes in PDOS of VTe_2 around the Fermi level.

S4–S9 within the SM [62]). Recently, 2D ferromagnetic metal Fe_3GeTe_2 has also been theoretically predicted to be a good OER catalyst [60]. In contrast, for 1T-CrX_2 and 1T-MnX_2, such a synergetic effect on the OH* or O* adsorption between the nearest neighboring M atoms to the adsorption site and

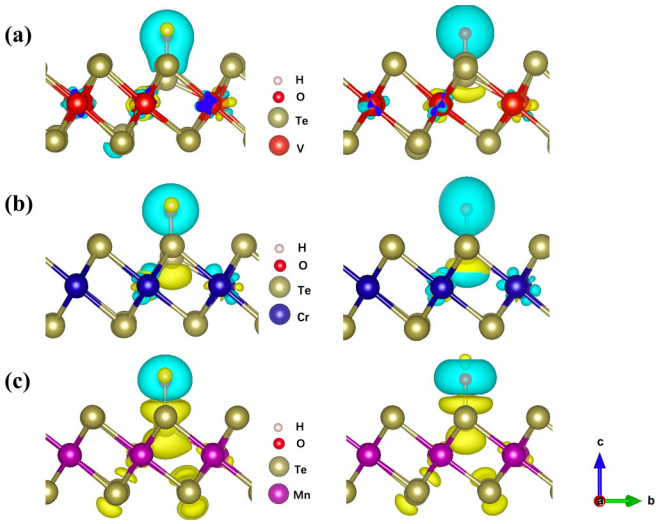

FIG. 9. Spin-density differences for adsorption of OH* (left panels) and O* (right panels) on (a) 1T-VTe_2, (b) 1T-$CrTe_2$ and (c) 1T-$MnTe_2$. Blue and yellow areas represent spin density decrease and spin density increase, respectively.

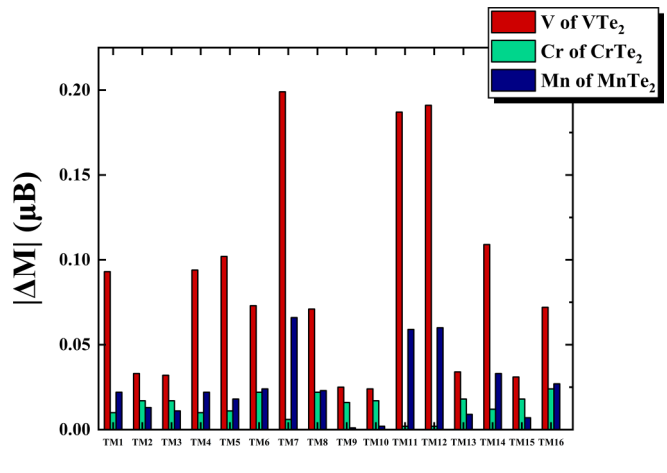

FIG. 10. Absolute values of the magnetic moment changes of 1T-MTe_2 upon the O* adsorption. The labels of the TM atoms correspond to Fig. S9 within the SM [62].

other M atoms is minor. By comparing Tables S6–S9 (see SM [62]) and Figs. 9(b) and 9(c), it is evident that only the three metal elements nearest to the adsorption site exhibit significant spin changes, nevertheless the metal elements far from the adsorption site remain basically unchanged. Note that the significantly reduced spin synergetic behavior involving neighboring M atoms from 1T-VX_2, through 1T-CrX_2, to 1T-MnX_2 seems highly correlated with their relative catalytic activities, which indicates again that synergistic effects of magnetism and *p-d* hybridization in the present systems significantly enhance their catalytic efficiencies. In addition, our calculations show that NM-VTe2 has poorer OER activity ($\eta_{\mathrm{OER}} = 0.61$ V) than the FM one ($\eta_{\mathrm{OER}} = 0.49$ V). To more directly reflect the importance of magnetism on the catalytic activity, we further examine whether the spin selection rule works in these systems, by taking the O* adsorption on 1T-VTe_2 as an example system. The total magnetic moments of the systems before and after adsorption are compared, showing that such a process obeys the spin selection rule. The detailed analysis is presented in Sec. S8 of the SM [62]. In general, the spin selection rule focuses on the single magnetic atom and the adsorbate, whereas for 1T-VTe_2, all the magnetic atoms should be considered due to their synergetic effect on the O* adsorption discussed above. The spin selection rule in the catalytic processes not only exhibits the limitation of the spin quantum number in the spin Hilbert subspace, but also greatly affects the charge reconstruction and transfer processes by influencing the spin variation. The existence of the spin selection rule also indicates different microscopic catalytic processes in the magnetic systems from those in the nonmagnetic systems.

IV. DISCUSSIONS AND CONCLUSIONS

Here we note that the *p-d* hybridization mechanism may prove to be generic in catalytic processes, applicable to both metallic and nonmetallic systems. Nevertheless, for the specific catalytic processes of HER and OER, the crucial step is for the H^+ or OH^- to respectively accept or donate an electron upon adsorption on the catalytic surface, which can more favorably take place on a metal system. We also recognize that the OER involves more complex intermediate steps, but abundant itinerant electrons of the catalyst are crucial for its overall efficiency [3].

To demonstrate the predictive power of the descriptor $\Delta_{\sigma\sigma^*}$, we now expand our searching for more systems that may have optimal HER efficiencies. These additional systems include two classes. The first class is the 1T-MX_2 (M = V, Cr, Mn; X = Se, Te) doped with different M atoms (Nb, Mo, Co, and Fe). The second is metal-N4@graphene systems [61]. For the doped 1T-MD systems, we expect that when doping leads to stronger *p-d* hybridization and lower p_z-band center, $\Delta\varepsilon_{p_z-H}$ and consequently $\Delta_{\sigma\sigma^*}$ will both be enlarged, resulting in a decrease in ΔG_{H^*}, and vice versa. In addition, in selecting a proper dopant, we ensure that no significant structural change takes place for the parent system and the atop adsorption of H* retains. The results are shown in Fig. S12 within the SM [62]. We find, indeed, doping $CrSe_2$ with Mo and doping $CrTe_2$ with V or Mo can enhance both $\Delta\varepsilon_{p_z-H}$ and $\Delta_{\sigma\sigma^*}$, the two obeying a linear scaling relation {Fig. S12(a) within the SM [62]}. Furthermore, when the results of ΔG_{H^*} for the doped systems are plotted together with those of the pristine systems, the data preserve the linear scaling between ΔG_{H^*} and $\Delta_{\sigma\sigma^*}$ [Fig. S12(b)], with several new desirable catalytic systems predicted for HER. Similar trends are also observed for the metal-N4@graphene systems, as depicted in Fig. S13 within the SM [62].

In summary, we have systematically investigated the catalytic properties of 1T-MX_2 for water splitting reactions. First, our comparative studies have shown that the ferromagnetic 1T-VSe_2 exhibits excellent HER catalytic activity. Through the combination analysis of charge density differences and PDOS, the p_z-band center of the X atoms has been demonstrated to dominate the H* adsorption and the *p-d* hybridization and magnetism synergistically enhance the HER catalytic performance of 1T-MX_2. We have proposed that $\Delta_{\sigma\sigma^*}$ can be used as a descriptor to characterize the HER activity and elucidated the corresponding physical origin. Next, we have shown that ferromagnetic 1T-VTe_2 possesses excellent OER catalytic performance. Due to the strong electronegativity of the O atoms, the systems with strong *p-d* hybridization can provide more abundant electronic states, which mainly affects the OER catalytic activity of 1T-MX_2. In addition, the spin selection rule has been observed upon O* adsorption on 1T-VTe_2, even though the local magnetic moment of each V atom changes significantly, indicating the importance of the spin degrees of freedom in the catalytic processes. Overall, this study has taken into account both orbital and spin degrees of freedom to explore the possible mechanisms in catalytic scenarios where the d-band model is not applicable, offering insights into the catalysis of two-dimensional magnetic materials.

ACKNOWLEDGMENTS

This work is supported by National Natural Science Foundation of China (Grants No. 11974323 and No. 12374458), the Innovation Program for Quantum Science and Technology (Grant No. 2021ZD0302800), the Strategic Priority Research Program of Chinese Academy of Sciences (Grant No. XDB0510200), and the Anhui Initiative in Quantum Information Technologies (Grant No. AHY170000).

[1] Y. Zheng, Y. Jiao, M. Jaroniec, and S. Z. Qiao, Advancing the electrochemistry of the hydrogen-evolution reaction through combining experiment, Angew Chem Int Ed **54**, 52 (2015).

[2] J. H. Montoya, L. C. Seitz, P. Chakthranont, A. Vojvodic, T. F. Jaramillo, and J. K. Nørskov, Materials for solar fuels and chemicals, Nat. Mater. **16**, 70 (2017).

[3] N.-T. Suen, S.-F. Hung, Q. Quan, N. Zhang, Y.-J. Xu, and H. M. Chen, Electrocatalysis for the oxygen evolution reaction: Recent development and future perspectives, Chem. Soc. Rev. **46**, 337 (2017).

[4] J. K. Nørskov, J. Rossmeisl, A. Logadottir, L. Lindqvist, J. R. Kitchin, T. Bligaard, and H. Jónsson, Origin of the overpotential

for oxygen reduction at a fuel-cell cathode, J. Phys. Chem. B **108**, 17886 (2004).

[5] J. K. Nørskov, T. Bligaard, A. Logadottir, J. R. Kitchin, J. G. Chen, S. Pandelov, and U. Stimming, Trends in the exchange current for hydrogen evolution, J. Electrochem. Soc. **152**, J23 (2005).

[6] J. Greeley, T. F. Jaramillo, J. Bonde, I. Chorkendorff, and J. K. Nørskov, Computational high-throughput screening of electrocatalytic materials for hydrogen evolution, Nat. Mater. **5**, 909 (2006).

[7] J. Suntivich, K. J. May, H. A. Gasteiger, J. B. Goodenough, and Y. Shao-Horn, A perovskite oxide optimized for oxygen evolution catalysis from molecular orbital principles, Science **334**, 1383 (2011).

[8] I. C. Man, H. Y. Su, F. Calle-Vallejo, H. A. Hansen, J. I. Martínez, N. G. Inoglu, J. Kitchin, T. F. Jaramillo, J. K. Nørskov, and J. Rossmeisl, Universality in oxygen evolution electrocatalysis on oxide surfaces, ChemCatChem **3**, 1159 (2011).

[9] Z. W. She, J. Kibsgaard, C. F. Dickens, I. Chorkendorff, J. K. Nørskov, and T. F. Jaramillo, Combining theory and experiment in electrocatalysis: Insights into materials design, Science **355**, aad4998 (2017).

[10] B. Hammer and J. K. Nørskov, Why gold is the noblest of all the metals, Nature (London) **376**, 238 (1995).

[11] B. Hammer, Y. Morikawa, and J. K. Nørskov, Co chemisorption at metal surfaces and overlayers, Phys. Rev. Lett. **76**, 2141 (1996).

[12] B. Hammer and J. Nørskov, Theoretical surface science and catalysis-calculations and concepts, in *Impact of Surface Science on Catalysis*, Advances in Catalysis Vol. 45 (Academic Press, New York, 2000), pp. 71–129.

[13] J. R. Kitchin, J. K. Nørskov, M. A. Barteau, and J. G. Chen, Role of strain and ligand effects in the modification of the electronic and chemical properties of bimetallic surfaces, Phys. Rev. Lett. **93**, 156801 (2004).

[14] T. Bligaard and J. Nørskov, Chapter 4 - Heterogeneous catalysis, in *Chemical Bonding at Surfaces and Interfaces*, edited by A. Nilsson, L. G. Pettersson, and J. K. Nørskov (Elsevier, Amsterdam, 2008), pp. 255–321.

[15] S. Bhattacharjee, U. V. Waghmare, and S.-C. Lee, An improved *d*-band model of the catalytic activity of magnetic transition metal surfaces, Sci. Rep. **6**, 35916 (2016).

[16] K. A. Stoerzinger, L. Qiao, M. D. Biegalski, and Y. Shao-Horn, Orientation-dependent oxygen evolution activities of rutile IrO_2 and RuO_2, J. Phys. Chem. Lett. **5**, 1636 (2014).

[17] A. Grimaud, K. J. May, C. E. Carlton, Y.-L. Lee, M. Risch, W. T. Hong, J. Zhou, and Y. Shao-Horn, Double perovskites as a family of highly active catalysts for oxygen evolution in alkaline solution, Nat. Commun. **4**, 2439 (2013).

[18] J. Hwang, R. R. Rao, L. Giordano, K. Akkiraju, X. R. Wang, E. J. Crumlin, H. Bluhm, and Y. Shao-Horn, Regulating oxygen activity of perovskites to promote NO_x oxidation and reduction kinetics, Nat. Catal. **4**, 663 (2021).

[19] L. Giordano, K. Akkiraju, R. Jacobs, D. Vivona, D. Morgan, and Y. Shao-Horn, Electronic structure-based descriptors for oxide properties and functions, Acc. Chem. Res. **55**, 298 (2022).

[20] J. T. Mefford, X. Rong, A. M. Abakumov, W. G. Hardin, S. Dai, A. M. Kolpak, K. P. Johnston, and K. J. Stevenson, Water electrolysis on $La_{1-x}Sr_xCoO_{3-\delta}$ perovskite electrocatalysts, Nat. Commun. **7**, 11053 (2016).

[21] H. Lee, O. Gwon, K. Choi, L. Zhang, J. Zhou, J. Park, J.-W. Yoo, J.-Q. Wang, J. H. Lee, and G. Kim, Enhancing bifunctional electrocatalytic activities via metal d-band center lift induced by oxygen vacancy on the subsurface of perovskites, ACS Catal. **10**, 4664 (2020).

[22] M. Liu, M. S. Hybertsen, and Q. Wu, A physical model for understanding the activation of MoS_2 basal-plane sulfur atoms for the hydrogen evolution reaction, Angew. Chem., Int. Ed. **59**, 14835 (2020).

[23] M. Deng, M. Xia, Y. Wang, X. Ren, and S. Li, Synergetic catalysis of *p-d* hybridized single-atom catalysts: First-principles investigations, J. Mater. Chem. A **10**, 13066 (2022).

[24] E. Wigner and E. E. Witmer, Über die Struktur der zweiatomigen Molekelspektren nach der Quantenmechanik, Z. Phys. **51**, 859 (1928).

[25] L. Österlund, I. Zorić, and B. Kasemo, Dissociative sticking of O_2 on Al(111), Phys. Rev. B **55**, 15452 (1997).

[26] J. Behler, B. Delley, S. Lorenz, K. Reuter, and M. Scheffler, Dissociation of O_2 at Al(111): The role of spin selection rules, Phys. Rev. Lett. **94**, 036104 (2005).

[27] J. Behler, B. Delley, K. Reuter, and M. Scheffler, Nonadiabatic potential-energy surfaces by constrained density-functional theory, Phys. Rev. B **75**, 115409 (2007).

[28] F. Libisch, C. Huang, P. Liao, M. Pavone, and E. A. Carter, Origin of the energy barrier to chemical reactions of O_2 on Al(111): Evidence for charge transfer, not spin selection, Phys. Rev. Lett. **109**, 198303 (2012).

[29] M. Kurahashi and Y. Yamauchi, Spin correlation in O_2 chemisorption on Ni(111), Phys. Rev. Lett. **114**, 016101 (2015).

[30] S. Li, X. Zhao, J. Shi, Y. Jia, Z. Guo, J. H. Cho, Y. Gao, and Z. Zhang, Interplay between the spin-selection rule and frontier orbital theory in O_2 activation and CO oxidation by single-atom-sized catalysts on TiO_2(110), Phys. Chem. Chem. Phys. **18**, 24872 (2016).

[31] M. C. Escaño and H. Kasai, A novel mechanism of spin-orientation dependence of O_2 reactivity from first principles methods, Catal. Sci. Technol. **7**, 1040 (2017).

[32] Y. Zhao, B. Li, R. Yin, Y. Wang, J. Yang, Z. Zhang, and B. Wang, Spin selection rule in single-site catalysis of molecular oxygen adsorption on transition-metal phthalocyanines, J. Phys. Chem. C **123**, 28158 (2019).

[33] F. A. Garcés-Pineda, M. Blasco-Ahicart, D. Nieto-Castro, N. López, and J. R. Galán-Mascarós, Direct magnetic enhancement of electrocatalytic water oxidation in alkaline media, Nat. Energy **4**, 519 (2019).

[34] Y. Sun, S. Sun, H. Yang, S. Xi, J. Gracia, and Z. J. Xu, Spin-related electron transfer and orbital interactions in oxygen electrocatalysis, Adv. Mater. **32**, 2003297 (2020).

[35] R. R. Chen, Y. Sun, S. J. H. Ong, S. Xi, Y. Du, C. Liu, O. Lev, and Z. J. Xu, Antiferromagnetic inverse spinel oxide $LiCoVO_4$ with spin-polarized channels for water oxidation, Adv. Mater. **32**, 1907976 (2020).

[36] W. Zhou, M. Chen, M. Guo, A. Hong, T. Yu, X. Luo, C. Yuan, W. Lei, and S. Wang, Magnetic enhancement for hydrogen evolution reaction on ferromagnetic MoS_2 catalyst, Nano Lett. **20**, 2923 (2020).

[37] Z. Li, Z. Wang, S. Xi, X. Zhao, T. Sun, J. Li, W. Yu, H. Xu, T. S. Herng, X. Hai *et al.*, Tuning the spin density of cobalt

single-atom catalysts for efficient oxygen evolution, ACS Nano **15**, 7105 (2021).

[38] X. Ren, T. Wu, Y. Sun, Y. Li, G. Xian, X. Liu, C. Shen, J. Gracia, H.-J. Gao, H. Yang, and Z. J. Xu, Spin-polarized oxygen evolution reaction under magnetic field, Nat. Commun. **12**, 2608 (2021).

[39] L. Zhang, X. Ren, X. Zhao, Y. Zhu, R. Pang, P. Cui, Y. Jia, S. Li, and Z. Zhang, Synergetic charge transfer and spin selection in CO oxidation at neighboring magnetic single-atom catalyst sites, Nano Lett. **22**, 3744 (2022).

[40] D. J. O'Hara, T. Zhu, A. H. Trout, A. S. Ahmed, Y. K. Luo, C. H. Lee, M. R. Brenner, S. Rajan, J. A. Gupta, D. W. McComb, and R. K. Kawakami, Room temperature intrinsic ferromagnetism in epitaxial manganese selenide films in the monolayer limit, Nano Lett. **18**, 3125 (2018).

[41] M. Bonilla, S. Kolekar, Y. Ma, H. C. Diaz, V. Kalappattil, R. Das, T. Eggers, H. R. Gutierrez, M.-H. Phan, and M. Batzill, Strong room-temperature ferromagnetism in VSe_2 monolayers on van der Waals substrates, Nat. Nanotechnol. **13**, 289 (2018).

[42] X. Zhang, Q. Lu, W. Liu, W. Niu, J. Sun, J. Cook, M. Vaninger, P. F. Miceli, D. J. Singh, S.-W. Lian *et al.*, Room-temperature intrinsic ferromagnetism in epitaxial $CrTe_2$ ultrathin films, Nat. Commun. **12**, 2492 (2021).

[43] B. Li, Z. Wan, C. Wang, P. Chen, B. Huang, X. Cheng, Q. Qian, J. Li, Z. Zhang, G. Sun *et al.*, van der Waals epitaxial growth of air-stable $CrSe_2$ nanosheets with thickness-tunable magnetic order, Nat. Mater. **20**, 818 (2021).

[44] P. Hohenberg and W. Kohn, Inhomogeneous electron gas, Phys. Rev. **136**, B864 (1964).

[45] W. Kohn and L. J. Sham, Self-consistent equations including exchange and correlation effects, Phys. Rev. **140**, A1133 (1965).

[46] G. Kresse and J. Furthmüller, Efficient iterative schemes for ab initio total-energy calculations using a plane-wave basis set, Phys. Rev. B **54**, 11169 (1996).

[47] P. E. Blöchl, Projector augmented-wave method, Phys. Rev. B **50**, 17953 (1994).

[48] G. Kresse and D. Joubert, From ultrasoft pseudopotentials to the projector augmented-wave method, Phys. Rev. B **59**, 1758 (1999).

[49] J. P. Perdew, K. Burke, and M. Ernzerhof, Generalized gradient approximation made simple, Phys. Rev. Lett. **77**, 3865 (1996).

[50] S. Grimme, J. Antony, S. Ehrlich, and H. Krieg, A consistent and accurate *ab initio* parametrization of density functional dispersion correction (DFT-D) for the 94 elements H-Pu, J. Chem. Phys. **132**, 154104 (2010).

[51] N. Lu, H. Guo, L. Li, J. Dai, L. Wang, W. N. Mei, X. Wu, and X. C. Zeng, MoS_2/MX_2 heterobilayers: Bandgap engineering via tensile strain or external electrical field, Nanoscale **6**, 2879 (2014).

[52] M. Kan, S. Adhikari, and Q. Sun, Ferromagnetism in MnX_2 (X = S, Se) monolayers, Phys. Chem. Chem. Phys. **16**, 4990 (2014).

[53] Z. Tang, Y. Chen, Y. Zheng, and X. Luo, Strain engineering magnetocrystalline anisotropy in strongly correlated VTe_2 with room-temperature ferromagnetism, Phys. Rev. B **105**, 214403 (2022).

[54] V. L. Deringer, A. L. Tchougréeff, and R. Dronskowski, Crystal orbital Hamilton population (COHP) analysis as projected from plane-wave basis sets, J. Phys. Chem. A **115**, 5461 (2011).

[55] W. Yu, J. Li, T. S. Herng, Z. Wang, X. Zhao, X. Chi, W. Fu, I. Abdelwahab, J. Zhou, J. Dan *et al.*, Chemically exfoliated VSe_2 monolayers with room-temperature ferromagnetism, Adv. Mater. **31**, 1903779 (2019).

[56] P. M. Coelho, K. Lasek, K. Nguyen Cong, J. Li, W. Niu, W. Liu, I. I. Oleynik, and M. Batzill, Monolayer modification of VTe_2 and its charge density wave, J. Phys. Chem. Lett. **10**, 4987 (2019).

[57] J. Hong, C.-J. Kang, and J. Kim, Role of electronic correlations in room-temperature ferromagnetism of monolayer $MnSe_2$, Phys. Rev. B **106**, 195428 (2022).

[58] W. Chen, J.-m. Zhang, Y.-z. Nie, Q.-l. Xia, and G.-h. Guo, Tuning magnetic properties of single-layer $MnTe_2$ via strain engineering, J. Phys. Chem. Solids **143**, 109489 (2020).

[59] W. Chen, J. min Zhang, Y. zhuang Nie, Q. lin Xia, and G. hua Guo, Electronic structure and magnetism of MTe2 (M = Ti, V, Cr, Mn, Fe, Co and Ni) monolayers, J. Magn. Magn. Mater. **508**, 166878 (2020).

[60] Y. Zhao, J. Gu, and Z. Chen, Oxygen evolution reaction on 2D ferromagnetic Fe_3GeTe_2: Boosting the reactivity by the self-reduction of surface hydroxyl, Adv. Funct. Mater. **29**, 1904782 (2019).

[61] Y. Wang and M. Shao, Theoretical screening of transition metal-N4-doped graphene for electroreduction of nitrate, ACS Catal. **12**, 5407 (2022).

[62] See Supplemental Material at http://link.aps.org/supplemental/10.1103/PhysRevB.109.195414 for the different adsorption sites in 1T-MX_2, PDOS changes of 1T-MX_2 in HER, free energies of the OER processes, etc.